GEOPHYSICS, VOL. 71, NO. 3 (MAY-JUNE 2006); P. V67–V77, 7 FIGS., 2 TABLES.
10.1190/1.2194511

Characterization of polarization attributes of seismic waves using continuous wavelet transforms

Mamadou S. Diallo[1], Michail Kulesh[1], Matthias Holschneider[1], Frank Scherbaum[2], and Frank Adler[3]

ABSTRACT

Complex-trace analysis is the method of choice for analyzing polarized data. Because particle motion can be represented by instantaneous attributes that show distinct features for waves of different polarization characteristics, it can be used to separate and characterize these waves. Traditional methods of complex-trace analysis only give the instantaneous attributes as a function of time or frequency. However, for transient wave types or seismic events that overlap in time, an estimate of the polarization parameters requires analysis of the time-frequency dependence of these attributes. We propose a method to map instantaneous polarization attributes of seismic signals in the wavelet domain and explicitly relate these attributes with the wavelet-transform coefficients of the analyzed signal. We compare our method with traditional complex-trace analysis using numerical examples. An advantage of our method is its possibility of performing the complete wave-mode separation/filtering process in the wavelet domain and its ability to provide the frequency dependence of ellipticity, which contains important information on the subsurface structure. Furthermore, using 2-C synthetic and real seismic shot gathers, we show how to use the method to separate different wave types and identify zones of interfering wave modes.

INTRODUCTION

Multicomponent seismic recording provides increased information for subsurface characterization, particularly in the estimation of the polarization states of seismic arrivals. The processing of such data sets is computationally expensive and requires sophisticated techniques in order to infer the physical properties and structure of the subsurface from the bulk of available information. With multicomponent data, usually one is confronted with the issue of separating seismic events of different polarization characteristics. For instance, one would like to distinguish between the body waves (P- and S-waves) that are linearly polarized from elliptically polarized Rayleigh waves. Polarization analysis is also used to identify shear-wave splitting (Rene et al., 1986; Li and Crampin, 1991).

Given a signal from three component recordings, with $S_x(t)$, $S_y(t)$, and $S_z(t)$ representing the seismic traces recorded in three orthogonal directions, any combination of two orthogonal components can be selected for the polarization analysis. Within the context of Rayleigh-wave characterization, one can select a combination of the vertical component $S_z(t)$ with the inline horizontal component (either $S_x(t)$ or $S_y(t)$). Note that sometimes obtaining the inline horizontal component requires an appropriate rotation of $S_x(t)$ and $S_y(t)$. Polarization analysis also can be carried out for all components simultaneously (Morozov and Smithson, 1996). Use of instantaneous attributes as defined by Taner et al. (1979) allows us to quantify the polarization of shear waves. Because Rayleigh waves are strongly dispersive in heterogeneous media, their polarization attributes are both frequency and mode dependent (Shieh and Herrmann, 1990). In the context of seismic-hazard assessment using ambient vibrations, the characterization of this frequency dependence is of enormous practical interest. Particularly in connection with dispersion measurements, the frequency dependence of the polarization of Rayleigh-wave packages in ambient vibration records can be used to help predict the shakeability of the corresponding subsurface structure (Scherbaum et al., 2003; Ohrnberger et al., 2003). In exploration seismology, however, Rayleigh-wave arrivals are considered to be coherent noises that must be filtered in order to enhance reflection events of interest.

René et al. (1986) proposed a method for multicomponent seis-

Manuscript received by the Editor July 4, 2003; revised manuscript received May 10, 2005; published online May 26, 2006.
[1]University of Potsdam, Applied and Industrial Mathematics, Am Neuen Palais 10, 14469, Potsdam, Germany. E-mail: mamadou.s.diallo@exxonmobil.com.
[2]University of Potsdam, Faculty of Geoscience, Karl-Liebnecht-Strasse 24-25, 14414 Potsdam, Germany. E-mail: fs@geo.uni-potsdam.de.
[3]University of Potsdam, Applied and Industrial Mathematics, am Neuen Palais 10, 14469, Potsdam, Germany. E-mail: adler@rz.uni-potsdam.de.

mic analysis based on complex-trace analysis (CTA). The method enables the computation of intantaneous polarization attributes that can be used to design filters for wavefield separation. However, since the CTA-based method operates only in the time domain, the computed attributes represent an average over all frequencies and therefore do not provide information about their frequency dependence.

In situations where the different wave types do not interfere in time, the CTA method does a good job in separating these wave types. However, in exploration seismic, such situations are rare, because strong Rayleigh-wave arrivals that obscure the reflection events of interest are always observed. It is difficult to remove the Rayleigh-wave mode from the horizontal- and vertical-shot gathers without compromising the continuity of the reflectors around the space and time windows where this wave interferes with reflection modes. This difficulty is because with CTA, zeroing time samples on the seismograms where the polarization parameters correspond to the events to be filtered not only removes the intrusive events but also information about the desired events at that point in time.

To address the limitations inherent to time-frequency resolution, we propose a method based on the continuous wavelet transform (CWT). Instead of eliminating Rayleigh waves by zeroing the wavelet coefficients corresponding to Rayleigh-wave energy (Shieh and Herrmann, 1990; Deighan and Watts, 1997) or by level-dependent thresholding (Abdu-Jauwad and Khene, 2000), we propose a mathematical model to characterize the elliptically polarized signal in the wavelet space. Given this mathematical tool, we recalculate those attributes defined by René et al. (1986) in the time-frequency domain. Using the wavelet-based method in this manner provides the possibility of separating all wave modes. We also show how to use the ellipticity attribute to gain some practical information from Rayleigh waves.

In the next section, we review the characteristics of polarized, multicomponent seismic data. We then introduce our approach to polarization analysis for 2-C seismic data in the time domain.

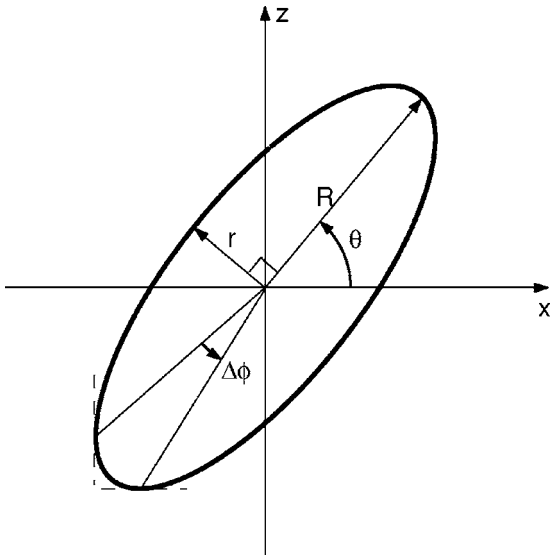

Figure 1. Schematic representation of an ellipse with its geometric parameters: the semimajor axis R, the semiminor axis r, the rise angle θ, and the phase difference $\Delta\phi$ between $S_x(t)$ and $S_z(t)$ components.

Thereafter, we present the extension of the method to the time-frequency domain using the continuous wavelet transform and derive an analytical expression to link the complex wavelet coefficients to the polarization attributes. Finally, using synthetic and real 2-C seismic data, we show how to use our method for the purpose of wavefield separation and surface-wave filtering.

LIST OF SYMBOLS

t	=	time
f	=	frequency
b	=	time location parameter
a	=	scale parameter
ω	=	instantaneous frequency
$\mathrm{mod}(x)$	=	modulo x
$(\cdot)^*$	=	complex conjugate
$S_k(t)$	=	channel of three-component recording. $k = x$-radial $k = y$-transversal, $k = z$-vertical component
$C(t)$	=	complex trace
$\mathcal{H}$	=	Hilbert transform
$(\hat{\cdot})$	=	Fourier transform
$C^+(t)$, $C^-(t)$	=	progressive and regressive complex traces, respectively
$\mathcal{W}_g C(b,a)$	=	wavelet transform of $C(t)$
$\mathcal{W}_g C^+(b,a)$, $\mathcal{W}_g C^-(b,a)$	=	progressive and regressive part of the wavelet transform
R, $R(t)$, $R(b,a)$	=	the semimajor axis as scalar, function of time and a function of time and frequency
r, $r(t)$, $r(b,a)$	=	the semiminor axis
θ, $\theta(t)$, $\theta(b,a)$	=	the rise angle
$\Delta\phi$, $\Delta\phi(t)$, $\Delta\phi(b,a)$	=	the phase-difference between $S_x(t)$ and $S_z(t)$ components
Ω, $\Omega(t)$, $\Omega(b,a)$	=	the angular frequency inside the polarization ellipse
Γ, $\Gamma(t)$, $\Gamma(b,a)$	=	the rotation frequency of the semimajor axis
$\rho(t)$, $\rho(b,a)$	=	reciprocal ellipticity
$\sigma(t)$, $\sigma(b,a)$	=	signed reciprocal ellipticity

COMPLEX ELLIPSES IN THE TIME DOMAIN

Our goal is to derive instantaneous polarization attributes from two seismic traces $S_x(t)$ and $S_z(t)$ corresponding to the horizontal (inline) and vertical components, respectively. We first define what we mean by pure elliptically polarized signals. In its full generality, an elliptically polarized rotating signal is described by four independent geometric parameters and two kinematic parameters (Figure 1):

1) R: the semimajor axis $R \geq 0$
2) r: the semiminor axis $r \geq 0$
3) θ: the rise angle, which is the angle of the semimajor axis with the horizontal x axis, $\theta \in (-\pi/2, \pi/2]$
4) $\Delta\phi$: the phase-difference between $S_x(t)$ and $S_z(t)$
5) Ω: the frequency inside the ellipse
6) Γ: the rotation frequency of the semimajor axis

Definition of instantaneous ellipticity

We now propose an alternative approach to the CTA for the definition of instantaneous polarization attributes. Consider two complex numbers A^+, A^- and two arbitrary real numbers ω^+, ω^-. Then consider the curve in the complex plane given by

$$C(\tau) = A^+ e^{i\omega^+\tau} + A^- e^{-i\omega^-\tau}. \tag{1}$$

We can rewrite the above equation as

$$C(\tau) = e^{i\Gamma\tau}(A^+ e^{i\Omega\tau} + A^- e^{-i\Omega\tau}), \quad \Gamma = (\omega^+ - \omega^-)/2, \quad \Omega = (\omega^+ + \omega^-)/2, \tag{2}$$

which corresponds to the equation of an ellipse rotating with the frequency Ω. The semimajor axis of this ellipse is also rotating but with the frequency Γ. Clearly, this interpretation is always mathematically exact, it is only visually valid in the case where $|\Gamma| \ll |\Omega|$. In the case $|\Gamma| \gg |\Omega|$; however, we have a circular movement with, frequency Γ and a radius that oscillates with the frequency Ω between the semiminor and semimajor axis. All geometric parameters may easily be computed as

$$\begin{aligned} R &= |A^+| + |A^-|, \\ r &= \big||A^+| - |A^-|\big|, \\ \theta &= \frac{1}{2}\arg(A^+A^-) \bmod \pi, \\ \Delta\phi &= \arg\frac{A^+ + (A^-)^*}{A^+ - (A^-)^*} + \frac{\pi}{2}. \end{aligned} \tag{3}$$

Complex trace

From the two traces $S_x(t)$ and $S_z(t)$ we form the complex trace

$$C(t) = S_x(t) + iS_z(t).$$

Generally, this signal is not analytic and thus has a prograde part $C^+(t)$ and retrograde part $C^-(t)$ so that

$$C(t) = C^+(t) + C^-(t), \tag{4}$$

where $C^\pm(t) = \frac{1}{2}(1 \pm i\mathcal{H})C(t)$.

Locally around t, we may write

$$C^+(t+\tau) \simeq C^+(t)e^{i\omega^+(t)\tau}, \quad C^-(t+\tau) \simeq C^-(t)e^{-i\omega^-(t)\tau}, \tag{5}$$

with $\omega^\pm(t) = \pm d\arg(C^\pm(t))/dt$ as the instantaneous frequencies of $C^\pm$ at time t. Therefore, we have locally

$$C(t+\tau) \simeq C^+(t)e^{i\omega^+(t)\tau} + C^-(t)e^{-i\omega^-(t)\tau}, \tag{6}$$

which describes a rotating ellipse.

To summarize, we may define all independent instantaneous attributes as functions of time:

$$\begin{aligned} R(t) &= |C^+(t)| + |C^-(t)|, \\ r(t) &= \big||C^+(t)| - |C^-(t)|\big|, \\ \theta(t) &= \frac{1}{2}\arg(C^+(t)C^-(t)) \bmod \pi, \\ \Omega(t) &= (\omega^+(t) + \omega^-(t))/2, \\ \Gamma(t) &= (\omega^+(t) - \omega^-(t))/2, \\ \Delta\phi(t) &= \arg(C^+(t) + (C^-(t))^*) \\ &\quad - \arg(C^+(t)) - (C^-(t))^*) + \pi/2. \end{aligned} \tag{7}$$

Note that for a turning ellipse, the rise angle and phase difference are not intrinsically defined. We therefore define these quantities via the nonturning ellipse $C(t)e^{-i\Gamma t}$. The rise angle in this definition corresponds to the rise angle in Rene et al. (1986).

Besides the instantaneous attributes $R(t)$, $r(t)$, $\theta(t)$, $\Omega(t)$, and $\Gamma(t)$, it is useful to introduce the derived characteristics such as the reciprocal ellipticity $\rho(t)$ and the signed reciprocal ellipticity $\sigma(t)$ (Smith and Ward, 1974), which we write again as

$$\rho(t) = \frac{r(t)}{R(t)}, \quad \sigma(t) = \mathrm{sign}[\Delta\phi(t)]\rho(t). \tag{8}$$

With some algebraic manipulations, we can express $C^+(t)$ and $C^-(t)$ in terms of $R(t)$, $r(t)$, and $\theta(t)$ as

$$\begin{aligned} C^+(t) &= [R(t) + r(t)]e^{i[\theta(t)+\theta_0(t)]}, \\ C^-(t) &= [R(t) - r(t)]e^{i[\theta(t)-\theta_0(t)]}, \end{aligned} \tag{9}$$

where $\theta_0(t) = \arg(C^+(t)/(C^-(t))/2$, and the algebraic value of $r(t)$ is considered ($r(t) = |C^+(t)| - |C^-(t)|$). From the above $C^+(t)$ and $C^-(t)$ expression, we can reconstruct the full complex trace using equation 4. As we will show in the next section, expressing the complex trace in terms of the polarization attributes allows the design of an effective filter for mode separation based on these attributes.

COMPLEX ELLIPSES IN THE CWT DOMAIN

We first give a short overview of the wavelet transform of a complex signal. The wavelet transform of $C(t)$ with respect to a wavelet $g(t)$ is defined as

$$\mathcal{W}_g C(b,a) = \int_{-\infty}^{+\infty} \frac{1}{a} g^*\left(\frac{t-b}{a}\right) C(t)dt, \tag{10}$$

where $g([t-b]/a)/a$ is a family of wavelet functions, generated from a mother wavelet g through dilation $a \in \mathbb{R}$ and translations $b \in \mathbb{R}$. Assuming that $g(t)$ is a band-limited wavelet with a central frequency f and a bandwidth Δf, a daughter wavelet $g_{a,b}(t)$ is a similar signal with a central frequency $f_a = f/a$. The relative bandwidth is constant for every derived daughter wavelet and equal to that of the mother wavelet so that

$$\frac{\Delta f_a}{f_a} = \frac{\Delta f/a}{f/a} = \frac{\Delta f}{f} = constant. \tag{11}$$

If we take a wavelet with a unit-central frequency, we can directly obtain the physical frequency by taking the inverse of the scale. Performing the wavelet transform of $C(t)$ with respect to $g^+(t)$, the progressive part of $g(t)$ (i.e., $\hat{g}(\omega) = 0, \omega < 0$), and with respect to $g^-(t)$, the regressive part of g (i.e., $\hat{g}(\omega) = 0, \omega > = 0$), where $g(t) = g^+(t) + g^-(t)$, we obtain $\mathcal{W}_g C^+(b,a)$ for the positive frequencies and $\mathcal{W}_g C^-(b,a)$ for the negative frequencies, respectively, and can express the complete wavelet transform of $C(t)$ with respect to g as

$$\begin{aligned}\mathcal{W}_g C(b,a) &= \mathcal{W}_{g^+} C(b,a) + \mathcal{W}_{g^-} C(b,a)\\ &= \mathcal{W}_g C^+(b,a) + \mathcal{W}_g C^-(b,a)\end{aligned} \tag{12}$$

(Holschneider, 1995). Note the equivalence between the sum of the wavelet transforms of $C(t)$ obtained with $g^+(t)$ and $g^-(t)$, on the one hand, and the sum of the wavelet transforms of $C^+(t)$ and $C^-(t)$ obtained with $g(t)$, on the other hand.

One can recover the signal from its wavelet transform as

$$C(t) = \frac{1}{C_{g,h}} \int_{-\infty}^{+\infty} \int_{-\infty}^{+\infty} \frac{1}{a} h\left(\frac{t-b}{a}\right) \mathcal{W}_g C(b,a) \frac{dbda}{a}, \tag{13}$$

where $C_{g,h}$ is a constant defined as

$$C_{g,h} = \int_0^{+\infty} (\hat{g}(\omega)\hat{h}(\omega) + \hat{g}(-\omega)\hat{h}(-\omega)) \frac{d\omega}{\omega}, \tag{14}$$

and where $h(t)$ is the synthesizing wavelet used for the inverse wavelet transform (Holschneider, 1995).

In our present wavelet-transform application, we will use the complex Morlet wavelet (see Appendix A) as the mother wavelet. It is important in the context of instantaneous attributes analysis to use complex wavelets (in contrast to the wavelet transform with real wavelet) because of the advantage of not distorting the phase content of the analyzed signal. One way to use wavelets to obtain a time-frequency dependent analysis of instantaneous polarization attributes is to apply the CTA technique to $\mathcal{W}_g S_x(\cdot,a)$ and $\mathcal{W}_g S_z(\cdot,a)$, where g is a progressive wavelet. Indeed, in view of equation 12, these are the filtered analytic signals associated with the original traces. We do not pursue this idea in this paper but rather propose a definition of instantaneous ellipticity given by equations 1–3, which yields an additional parameter to describe local polarization attributes.

Instantaneous polarization attributes in the CWT domain

Until now we only have used the signal in its temporal representation to determine a time-varying instantaneous ellipticity. We now may use the wavelet transform to define a time-frequency dependent, instantaneous ellipticity. Using equation 12 to introduce the instantaneous frequency for scale and translation parameters (b,a) via

$$\omega^{\pm}(b,a) = \pm\, \partial_b \arg \mathcal{W}_g C^{\pm}(b,a), \tag{15}$$

we may write locally

$$\begin{aligned}\mathcal{W}_g C(b+\tau,a) \simeq\ & \mathcal{W}_g C^+(b,a) e^{i\omega^+(b,a)\tau}\\ &+ \mathcal{W}_g C^-(b,a) e^{-i\omega^-(b,a)\tau}.\end{aligned} \tag{16}$$

Again, we discover the geometry of a rotating ellipse at each point (b,a). The geometric and kinematic parameters may be computed as

$$\begin{aligned}R(b,a) &= |\mathcal{W}_g C^+(b,a)| + |\mathcal{W}_g C^-(b,a)|,\\ r(b,a) &= ||\mathcal{W}_g C^+(b,a)| - |\mathcal{W}_g C^-(b,a)||,\\ \theta(b,a) &= \frac{1}{2}\arg(\mathcal{W}_g C^+(b,a)\mathcal{W}_g C^-(b,a)),\\ \Omega(b,a) &= \frac{1}{2}\partial_b \arg(\mathcal{W}_g C^+(b,a)/\mathcal{W}_g C^-(b,a)),\\ \Gamma(b,a) &= \frac{1}{2}\partial_b \arg(\mathcal{W}_g C^+(b,a)\mathcal{W}_g C^-(b,a)),\\ \Delta\phi(b,a) &= \arg\left[\frac{\mathcal{W}_g C^+(b,a) + (\mathcal{W}_g C^-(b,a))^*}{\mathcal{W}_g C^+(b,a) - (\mathcal{W}_g C^-(b,a))^*}\right] + \frac{\pi}{2}.\end{aligned} \tag{17}$$

We thus have defined at each point in the wavelet space an instantaneous ellipse characterizing the polarization attributes of the pair $S_x(t)$ and $S_z(t)$ at each time and at each frequency.

Before we embark on the analysis, it is important to emphasize that the instantaneous attributes defined above do not provide any information on the polarization unless they are observed for a certain time and frequency window. Displaying any attribute in the frequency-time space would primarily serve to identify coherent structures that belong to the same seismic event before proceeding with the analysis of its average in either the time or the frequency domain.

Back to time domain

One way to reconstruct time-dependent quantities from the wavelet coefficients is to average the above formulas over suitable regions (Torrence and Compo, 1998) in which a seismic event has been identified in wavelet space. A second method is based on the ridge functions of both $\mathcal{W}_g C^+(b,a)$ and $\mathcal{W}_g C^-(b,a)$ (Torrésani, 1995). Given the wavelet transform $\mathcal{W}_g C^{\pm}(b,a)$ of the complex signal $C(t)$, the wavelet ridges are defined as the set of points (b,a) on the phase plane where

$$\frac{\partial \arg \mathcal{W}_g C^{\pm}(b,a)}{\partial b} = \frac{\omega_0}{a^{\pm}}, \tag{18}$$

and where ω_0 is the central frequency of the analyzing wavelet.

If we can identify the two ridges $a^{\pm}(b)$, one of which is for the progressive and the other for the regressive part, the restriction of the wavelet transforms to these lines will yield instantaneous ellipticity parameters as a function of time b. This would allow us to extract all the information related to the elliptical propagation of a Rayleigh wave. Then we can further exploit these attributes for the design of a Rayleigh-wave filtering algorithm. This approach is good as long as the ridge remains near horizontal so that the rela-

tion between the ridge function and the instantaneous frequency is valid. This corresponds to the case of slowly varying ellipses.

A third approach that leads to a systematic design of wave-mode filtering/separation can be developed. This approach is based on the explicit relation between the complex trace and polarization attributes (see above subsection). Notice that equation 12 is the wavelet transform of equation 4. As in equation 9, we can express $\mathcal{W}_g C^+(b,a)$ and $\mathcal{W}_g C^-(b,a)$ in terms of the polarization attributes $\theta(b,a)$, $R(b,a)$ as

$$\mathcal{W}_g C^+(b,a) = [R(b,a) + r(b,a)]e^{i[\theta(b,a)+\theta_0(b,a)]},$$
$$\mathcal{W}_g C^-(b,a) = [R(b,a) - r(b,a)]e^{i[\theta(b,a)-\theta_0(b,a)]}, \quad (19)$$

where $\theta_0(b,a) = \arg[\mathcal{W}_g C^+(b,a)/\mathcal{W}_g C^-(b,a)]/2$ and $r(b,a) = |\mathcal{W}_g C^+(b,a)| - |\mathcal{W}_g C^-(b,a)|$.

Given the above equations, we can perform the filtering/wave-modes separation using selective criteria that involve the reciprocal ellipticity $\rho(b,a)$ and the rise angle $\theta(b,a)$. For instance, to extract the Rayleigh waves from an observed seismogram, we can select a certain range of $R(b,a)$ and $r(b,a)$, based on the observed value of $\rho(b,a)$ and the rise angle $\theta(b,a)$ at the points (b,a) on the phase plane, and set the values of respective polarization attributes outside this selected range to zero. Such an operation would result in filtered polarization attributes that explicitly model the Rayleigh-wave arrivals. The next step will consist of recasting these filtered attributes into equation 19 and adding the result to get the wavelet coefficients of the filtered wavelet transform in the form of equation 12. Then one gets the two filtered components of the complex trace in the time domain by performing an inverse wavelet transform on these wavelet coefficients. From this illustration, we see that extracting/filtering specific wave modes simply becomes a matter of tuning the polarization parameters to meet preset criteria specific to the wave mode of interest.

The advantage of the present approach over the second method is that it can be applied more systematically because the tuned polarization parameters for a specific mode are unique for all traces in the actual seismic section. For the second method, obtaining the ridges requires analysis of the seismic data on a trace-to-trace basis because the characteristic of the ridges can change significantly from one station to another. For a detailed analysis over a limited number of traces, the ridge approach may yield good results. However, the cost of its use becomes prohibitive as soon as the data volume increases (e.g., analysis of a whole seismic section). The same remarks apply with respect to the averaging approach as for the comparison of the third approach with the ridges-detection approach. However, we expect the ridge method to perform much better than the averaging method because it is more flexible and requires less interpretation.

Back to the frequency domain

Similar to the derivation of time-dependent attributes in the previous section, one also may perform an averaging of the wavelet attributes along the parameter b and obtain a smoothed version of the Fourier transform of each attribute (Torrence and Compo, 1998). Such an averaging would not offer any additional advantage over the CTA.

Considering the second method discussed in the previous section, reading R and r at ridge points as a function of frequency is useful because this information can be combined with the signed phase difference to detect the frequency at which the change between prograde/retrograde occurs with Rayleigh waves. The determination of this frequency is of practical importance in near-surface investigation using Rayleigh waves (Scherbaum et al., 2003; Ohrnberger et al., 2003).

One can estimate this frequency with the help of the horizontal-to-vertical spectral ratios (H/V method), which are used often to analyze ambient vibrations. The basic assumption underlying its interpretation in practice is that ambient vibration signals are dominated (at least at times) by Rayleigh waves. While this assumption has been controversial, it is now commonly accepted within the scientific community (Bard, 1998). Strong support comes from array measurements of vertical component records that show a clear dispersion in certain frequency bands and propagation velocities corresponding to Rayleigh waves (Scherbaum et al., 2003). Therefore, during those time windows in which Rayleigh waves dominate, H/V spectral ratios are essentially sampling Rayleigh-wave ellipticities in a statistical sense.

For a situation in which a low-velocity layer (e.g., soft soil) overlays a more rigid basement, the vertical component of the Rayleigh wave will not be amplified as much as the horizontal one. This effect is frequency dependent with the modulus of the Rayleigh-wave ellipticity exhibiting a peak roughly at the fundamental S-wave resonance frequency of the layer (Lachet and Bard, 1994; Scherbaum et al., 2003). These peak frequencies contain important constraints on the subsurface velocity structure, especially the traveltime within the surface layer (Scherbaum et al., 2003). Therefore, in situations where the shear wave velocities of the surface layer are known, peak frequencies of H/V ratios can provide a quick and easy method to determine the thickness of soft deposits (Scherbaum et al., 2003). This approach is used increasingly in the context of seismic hazard assessment and the prediction of local site effects during strong earthquakes.

For the third approach, used to separate different wave modes in a more systematic manner, one can get a smoother Fourier transform of the filtered event. This is achieved through an appropriate averaging of the filtered wavelet coefficient along the time scale b.

EXAMPLES

For the following example, we generate synthetic 2-C seismograms. These seismograms are computed for an impulsive force acting on the surface of a single layer over a half-space model using the modal-summation method of Herrmann (1996). The model parameters are given in Table 1.

Table 1. Elastic parameters used for the synthetic seismogram computation. *Vp* and *Vs* are the compressional and shear velocities, respectively. ρ is the density; *Qp* and *Q*s are the quality factors. The source-receiver distance is 1.2 km.

Thickness	*Vp*(m/s)	*Vs*(m/s)	$\rho(kg/m^3)$	*Qp*	*Qs*
50	1350	200	1.9	30	10
∞	2000	1000	2.5	300	100

Simulated real seismogram with Rayleigh-wave arrivals

Figure 2a shows the computed vertical and horizontal components. The large-amplitude wave package arriving after approximately 3.5 s is produced predominantly by the fundamental-mode Ray-leigh-wave component, while the body-wave contributions arrive at earlier times.

The wavelet transform image in Figure 2b indicates that there is an overlap of the frequency windows of the body and Rayleigh waves. Notice the strength and continuity of the elongated event between 3.8 s and 6 s, which covers the Rayleigh-wave arrival. Also superimposed on Figure 2b is a curve that shows the location of the maxima for both regressive and progressive parts of the wavelet transform.

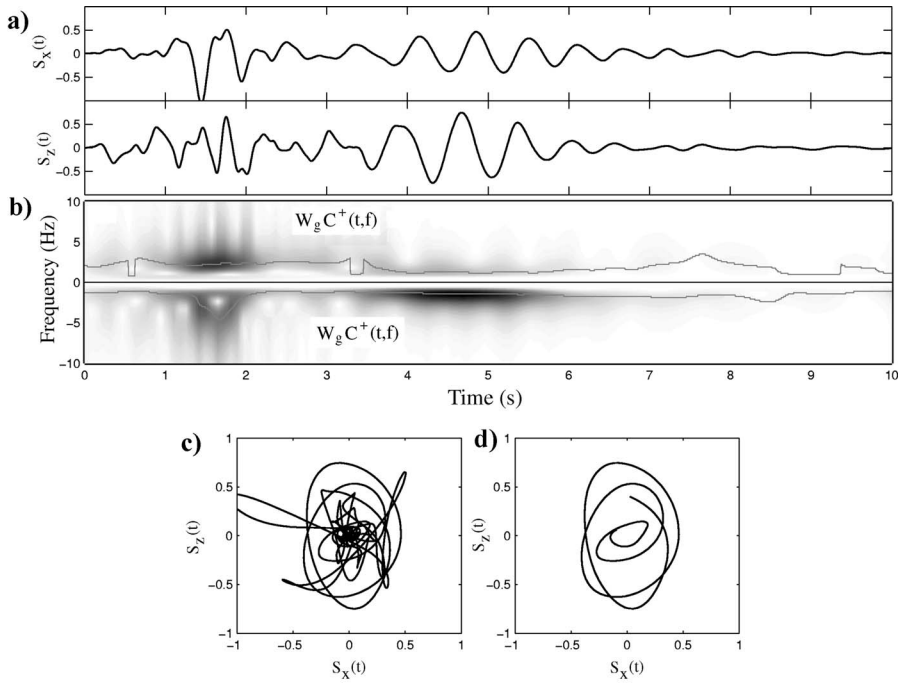

Figure 2. (a) Components of the synthetic 2-C seismograms. (b) Its progressive and regressive wavelet transform. (c) Hodogram showing the particle motion over the entire time window. (d) Hodogram for the time window of the Rayleigh-wave arrival between 3.8 s and 8 s.

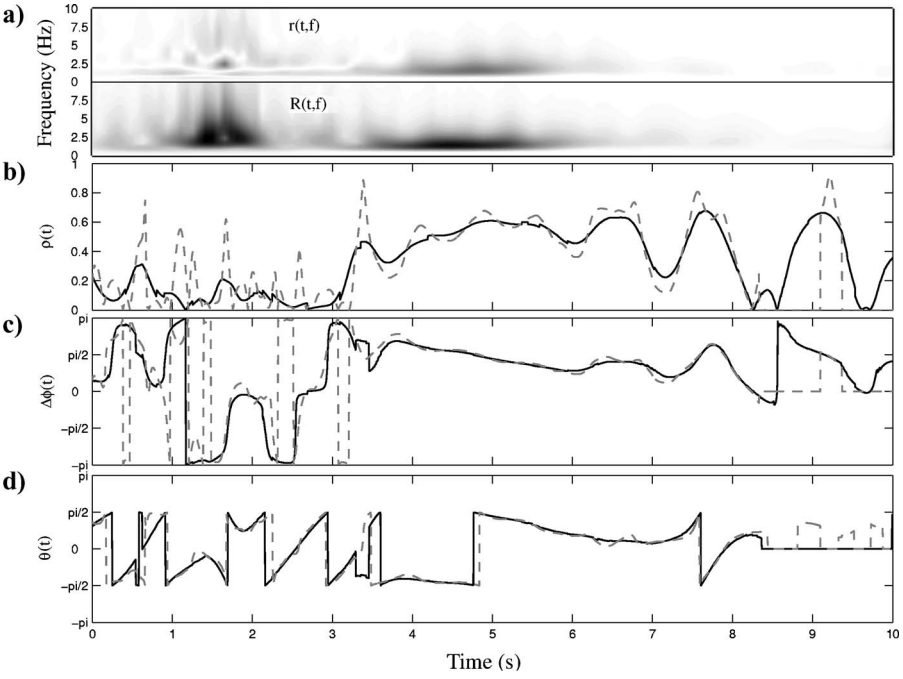

Figure 3. (a) The semimajor and semiminor axes in time-frequency domain obtained from the present study for the synthetic seismograms in Figure 2a. (b) The corresponding reciprocal ellipticity. (c) The phase difference between the two components. (d) The rise angle. The dashed lines correspond to the CTA method, while the solid lines show the values obtained from the present study.

Figure 2c shows particle motion over the full time window. In Figure 2d, the particle-motion plot is restricted to the time window between 3.8 s and 6 s where one can recognize the nearly vertical, elliptical structures related to Rayleigh waves. The rise angle of the Rayleigh ellipse may oscillate between $-\pi/2$ and $\pi/2$ radians. This is the case for the present example, as evidenced by the hodogram plot and the rise angle that averages to nearly $-\pi/2$ and $\pi/2$ within the Rayleigh-arrival window. The slight departure from the expected angles of $-\pi/2$ is caused by the deformation of the instantaneous ellipses. This, in turn, affects the instantaneous orientation of the ellipse. This variation in the instantaneous ellipse orientation explains the changing sign in rise angle observed around 5 s on the time axis.

The attribute plots in Figure 3 display some striking features. First, notice a relatively smooth variation that is consistent across all attributes in the time window from 3 s to 7 s, in contrast to wild oscillations outside this time frame (i.e., the region of the body waves or the tail of the seismic traces where S/N is very weak). The variation of the reciprocal ellipticity plot in Figure 3b from 3.8 s to 6 s is generally consistent with the shape of the ellipses in Figure 2d. With this attribute, both the wavelet-based method and the CTA show a clear distinction between linear and elliptical polarized arrivals, which is marked by the sharp increase in $\rho(t)$ around the onset time of the Rayleigh-wave arrival. For the present study, $\rho(t)$, $\Delta\phi(t)$, and $\theta(t)$ in Figure 3 were obtained using the Ridge method (equation 18). From the different numerical illustrations, one can recognize the excellent agreement between the CTA (dashed lines) and the present study (solid lines) as far as the ellipticity-attribute determination is concerned.

To compare the ellipticity from H/V and the new method, we consider separately the fundamental mode contribution to the complete seismogram. In Figure 4, we compare the variation of ellipticity in time and frequency (determined by the wavelet-based method) with what we would theoretically expect for the fundamental mode. Figure 4a shows the theoretical temporal variation of $\rho(\omega)$ as a function of group arrival time (dashed line) from H/V in comparison to the wavelet-based result (solid line). The change between prograde/retrograde motion is well detected in Figure 4b, as is the general trend of the temporal behavior. With respect to the frequency dependence shown in Figure 4a, the wavelet-based method performs even better. The theoretical H/V-spectral ratio exhibits a peak at 1 Hz, which is replicated fairly well by the ellipticity parameter from the present method. This is clearly another advantage of the wavelet-based method over the CTA. The latter method cannot obtain the frequency-dependent ellipticity.

APPLICATIONS TO 2-C SYNTHETIC DATA AND 2-C REAL DATA FROM FORT WORTH, TEXAS, U. S. A.

Analysis of the synthetic 2-C data set

Issues of interest in exploration geophysics are the identification and interpretation of polarized events from multicomponent data. To address these issues, we separate polarized events from a 2-C elastic synthetic example from the Fort Worth Basin, U. S. A. Figures 5a and 5b show the shot gathers for the inline horizontal and vertical components. The identification of polarized events in these synthetics is complicated by the presence of considerable interfering events, such as P- and S-waves with backscattered head waves. The synthetics also contain converted as well as surface waves. Details about the construction of the model and synthetic generation are available in Gherasim et al. (2004).

Figures 5c and 5d show plots for the reciprocal ellipticity and the rise angle for the Fort Worth data computed with the CTA (equation 7). From these two plots we can identify the polarization characteristics of the prominent wave modes present in the synthetics. For example, in Figure 5c, linearly polarized events are marked by red to yellow colors corresponding to small reciprocal ellipticity values (e.g., $\rho \in [0\ .\ .\ .\ 0.2]$). The continuous red events on this plot correlate well with the reflection modes from both the inline horizontal and vertical components. Note the pink-blue events corresponding to the Rayleigh-wave arrivals in Figure 5d, evidenced by values of the rise angle corresponding to that event and quite close to $|\pi/2|$. The combined interpretation of these two plots allows us to identify the vertically polarized reflections (P-wave, red in both Figures 5c and 5d) from those with horizontal polarization (S-Wave, red in Figure 5c but light-blue in 5d).

In the following example, 2-C synthetic shot gathers are analyzed with our wavelet-based method. The shot gathers were filtered with different sets of $\rho(b,a)$ and $\theta(b,a)$ (as indicated in Table 2) and delimited by the threshold values $\rho_f = 0.15$ and $\theta_f = 0.7$. Filtering was implemented with each set so that a particular polarization type either can be filtered out or kept in the final seismograms; as such, we can effectively identify different interfering events.

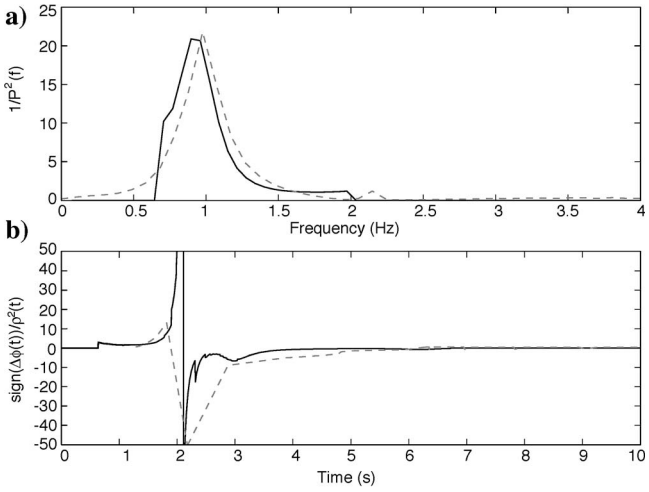

Figure 4. (a) Variation of the signed ellipticity versus frequency and (b) ellipticity versus time. The dashed lines show the theoretical values, while the solid lines show the values obtained from the present study.

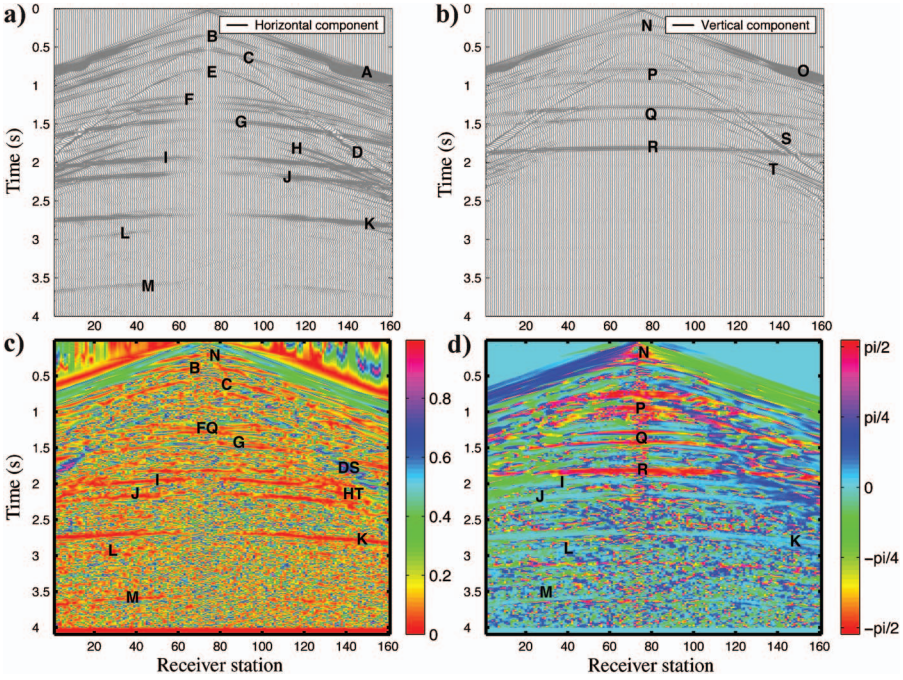

Figure 5. 2-C elastic synthetic seismogram from the Fort Worth Basin. (a) The horizontal component. (b) The vertical component. (c) Computed reciprocal ellipticity from the CTA. (d) Computed rise angle form the CTA.

Figures 6a and 6b show the result of the analysis where the linear and horizontally polarized wave mode is enhanced. Because the analysis is carried out with inline horizontal and vertical components, such a wave mode will be dominated by the SV-wave type. As we see from the horizontal component, all the reflection modes that were interpreted as horizontally polarized from the color-coded display of the CTA parameters (Figures 5c and 5d) are significantly enhanced, and the mode identified as Rayleigh wave is strongly attenuated. On the vertical component, which is normally dominated by the compressional mode at near offset, all wave modes have been drastically attenuated except for some relatively strong events at far-offset receivers, observed between 1.6 s and 2.2 s. These are SV events captured by the vertical component at far offset. Note the elimination of the first arrivals at far offset corresponding to the backscattered head waves.

Table 2. Classification of wave modes using the polarization attributes.

Filter name	Filter denotation	$\rho(b,a)$	$\theta(b,a)$
Linear and horizontally polarized	LH	$\rho \notin [\rho_f \; . \; . \; 1-\rho_f]$	$\lvert\theta\rvert < \theta_f$
Linear and vertically polarized	LV	$\rho \notin [\rho_f \; . \; . \; 1-\rho_f]$	$\lvert\theta\rvert \geq \theta_f$
Elliptic and horizontally polarized	EH	$\rho \in [\rho_f \; . \; . \; 1-\rho_f]$	$\lvert\theta\rvert < \theta_f$
Elliptic and vertically polarized	EV	$\rho \in [\rho_f \; . \; . \; 1-\rho_f]$	$\lvert\theta\rvert \geq \theta_f$

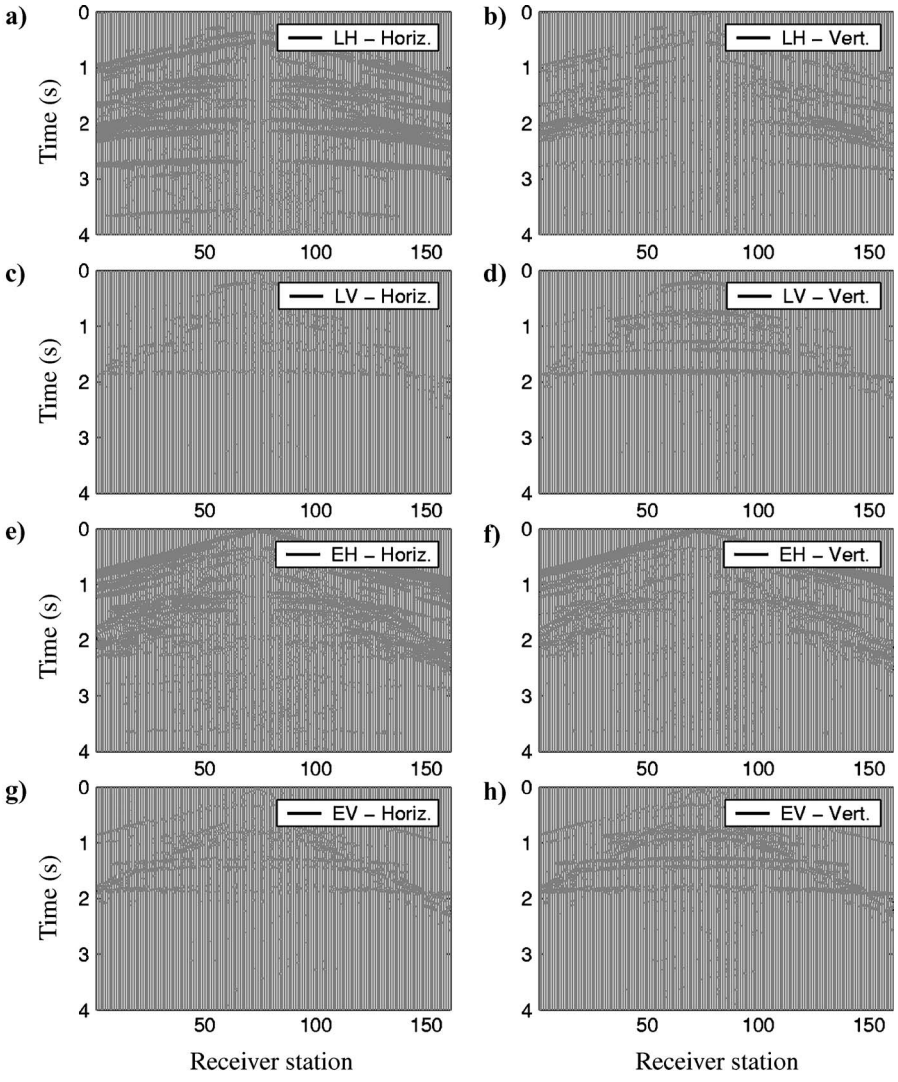

Figure 6. Separation of wave modes present in the 2-C elastic synthetic seismogram from the Fort Worth Basin by application of the different filter sets, denoted by LH, LV, EH, and EH, with $\rho_f = 0.15$ and $\theta_f = 0.7$.

We next consider the analysis for the case of linear and vertically polarized wave mode. The result is shown in Figures 6c and 6d for the horizontal and vertical components, respectively. All wave modes have been significantly attenuated on the horizontal component. This attenuation effect seems to be particularly strong for the far offset. Because P and SV displacements are in the vertical *x*-*z* plane, both P- and SV-waves have horizontal and vertical components when the angle of incidence is not 0° or 90°. The weak events on the horizontal shot gather correspond to P-wave reflections recorded on the horizontal component. In contrast, the vertical component shows a strong reflection mode around 2 s in time. Observe that those reflection events, partially visible later in time in the original vertical component, are not present anymore. What we actually see in this filtered shot gather are enhanced P-P reflections. Note the high-frequency nature of these events in comparison to those of the shear-wave modes in Figure 6a. For this particular polarization parameters setting, arrivals at far offset are attenuated rather simply because the particle motions of the P-P events, predominantly in the vertical z direction in the near offset, will shift toward the horizontal direction at far offset and therefore cannot be sensed by the vertical component.

We turn now to the third wave-mode classification criterion. The results of applying the corresponding filter, denoted as EH in Table 2, are depicted in Figures 6e and 6f. With this filter, we seek to detect those modes with elliptic and horizontal polarization. The most striking features in the vertical and inline-horizontal filtered shot gathers for these modes are the high-amplitude first arrivals with relatively low frequency, particularly at far offsets, and the absence of the reflection modes below 2 s in time. Additionally, events in the filtered inline-horizontal component have larger amplitudes than corresponding events on the filtered vertical component. This observation suggests

that the enhanced events most likely occur at locations predominantly affected by interferences of converted P to SV, with the pure SV.

With the fourth classification criterion, denoted as elliptic and vertically polarized, we normally emphasize the occurrence of the usual Rayleigh wave and expect the locations of enhanced events to be close in both space and time. The filtered shot gathers for this case are shown in Figures 6g and 6h. In contrast to the previous case, however, we no longer observe the energetic low-frequency first arrivals. Moreover, the overall frequency content of the enhanced events is relatively higher. Note also that the amplitude strength is dominated by the events in the vertical component, suggesting that the observed modes are the result of interfering P- and SV-waves converted to P-waves. Here, the Rayleigh wave again can be easily observed.

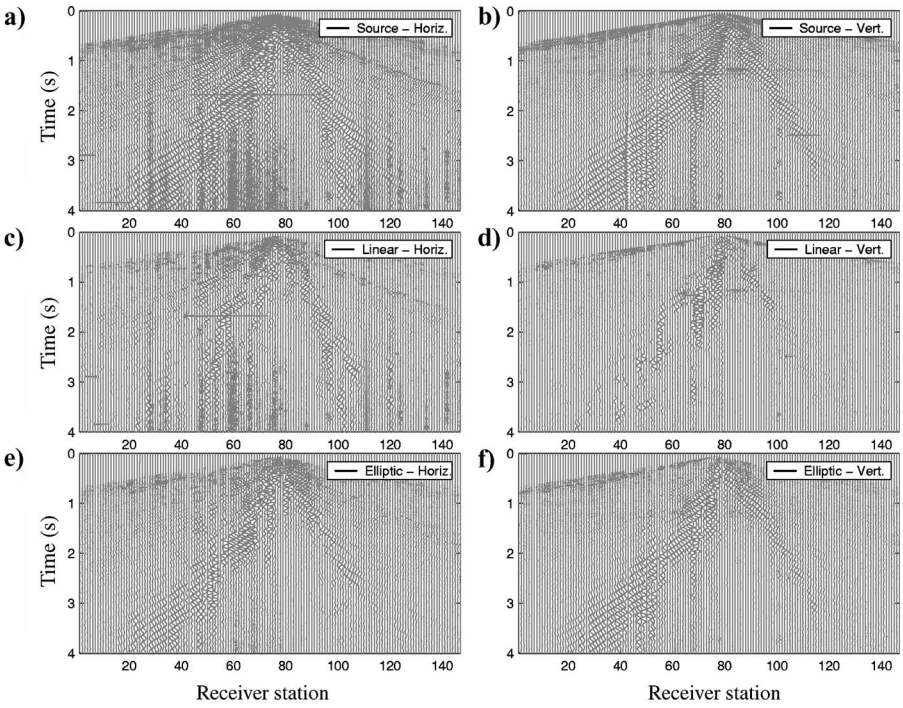

Figure 7. Real 2-C shot gather from Forth Worth Basin. (a) The horizontal component. (b) The vertical component. (c)–(d) Filtered real shot gathers showing the overall linearly polarized events (combined LH and LV filter). (e)–(f) Filtered real shot gathers showing the overall elliptically polarized events (combined EH and EV). $\rho_f = 0.15$ and $\theta_f = \pi/2$ because no distinction is made between horizontal and vertical polarization.

Real 2-C component data set

Finally, to test the performance of our method in filtering Rayleigh waves, we applied the method to the raw 2-C data from Fort Worth Basin U. S. A., shown in Figure 7. Because the data were not yet edited and preprocessed, we cannot carry out detailed interpretation in terms of wave mode as we did for the synthetics. As such, we limit ourselves to a qualitative appraisal of our method in separating the Rayleigh waves from the overall linearly polarized signals (i.e., combined LH & LV). The results for the linearly polarized events are shown in Figures 7c and 7d, where wave packets corresponding to the elliptically polarized events (Rayleigh waves among others) have been significantly attenuated. In contrast, Figures 7e and 7f show where wave packets are enhanced. Note the improved resolution for the high-frequency event on the vertical component to the right of the receiver at station 80 and between 1 s and 1.5 s in time.

CONCLUSIONS

We propose a method for computing instantaneous attributes of multicomponent signals using the continuous wavelet transform. The advantage of this method over previous techniques is that both time and frequency dependence of the attributes can be obtained. This allows one to separate events that have the same arrival times but different frequency content, or conversely, events with the same frequency content but arriving at different times. Various numerical examples show a good agreement between CTA and the wavelet method, with the latter less prone to unexpected fluctuations of attributes. One important improvement of the new method is its ability to provide a means to investigate the frequency dependence of all attributes. A practical application of such information is the determination of the fundamental frequency of a soft surface layer, which can be obtained from the peak of the frequency-dependent ellipticity. Good agreement between the new and H/V methods was observed in the numerical example.

The fact that the time-frequency dependent attributes are explicitly related to the wavelet transform of the signals enables us to perform the wave mode separation in the wavelet domain. With an appropriate tuning of the filter used to separate the wave modes, it also is possible to detect the regions of interfering wave modes. Application of our method to synthetic and real 2-C data for wave mode separation provided encouraging results. Our methodology can be easily extended to the analysis of multicomponent data from VSP and OBC surveys.

ACKNOWLEDGMENTS

This project is supported by a grant from the Deutsche Forschung Gemeinschaft (DFG) within the framework of the priority program 1114, “Mathematical methods in time series analysis and image processing.” We thank two anonymous reviewers and associate editor Kurt J. Marfurt for their helpful and constructive comments. We are especially grateful to the associate editor who pointed out some potential applications of our wavelet-based method and for providing the 2-C synthetic and real data set from the Fort Worth Basin. We also thank Matthias Ohrnberger (Geoscience faculty, University of Potsdam) for his contributions to the generation of the synthetic real seismograms in Figure 2, Christian Haberland (Geoscience faculty, University of Potsdam) for the conversion of the SEGY data, and Warren Ross (ExxonMobil Upstream Research Company) for reviewing the final manuscript to improve its readability.

APPENDIX A
WAVELET THEORY

In the following appendix, we restate clearly the basic formulas of wavelet analysis used in our polarization application. The wavelet transform of a signal $s(t)$ with respect to a wavelet $g(t)$ is defined in terms of the scalar product in $L^2(\mathbb{R})$ (Holschneider, 1995) as

$$\mathcal{W}_g s(b,a) = \int_{-\infty}^{+\infty} \frac{1}{a} g^*\left(\frac{t-b}{a}\right) s(t)dt = (g_{b,a}, s), \tag{A-1}$$

where $g_{a,b}(t) = g([t-b]/a)/a$ is a family of wavelet functions generated from a mother wavelet g through dilation ($a > 0$) and translations $b \in \mathbb{R}$. The half-plane of dilations and translations is denoted as $H = \{(b,a): b \in \mathbb{R}, a > 0\}$.

Assuming that $g(t)$ is a band-limited wavelet with a central frequency f and a bandwidth Δf, a daughter wavelet $g_{a,b}(t)$ is a similar signal with a central frequency $f_a = f/a$. The relative bandwidth is constant for every derived daughter wavelet and equal to that of the mother wavelet, so that

$$\frac{\Delta f_a}{f_a} = \frac{\Delta/a}{f/a} = \frac{\Delta f}{f} = constant. \tag{A-2}$$

If we introduce the Fourier transform pair

$$\hat{s}(\omega) = \int_{-\infty}^{+\infty} e^{-i\omega t} s(t)dt, \quad s(t) = \frac{1}{2\pi}\int_{-\infty}^{+\infty} e^{i\omega t}\hat{s}(\omega)dt, \tag{A-3}$$

then the wavelet transform may be written using Parseval's equation

$$\mathcal{W}_g s(b,a) = \frac{1}{2\pi}\int_{-\infty}^{+\infty} \hat{g}^*(a\omega) e^{ib\omega}\hat{s}(\omega)d\omega. \tag{A-4}$$

From this we see that the inverse of the scale $1/a$ may be associated with a frequency measured in units of the central frequency of g.

A wavelet $g \in L^2(\mathbb{R})$ is called admissible (with respect to all frequencies) if we have

$$C_g^{\pm} = \int_0^{\infty} |\hat{g}(\pm\omega)|^2 \frac{d\omega}{\omega} < \infty. \tag{A-5}$$

It is called admissible with respect to positive (negative) frequencies if $C_g^+ < \infty$ and $C_g^- = 0$ ($C_g^+ = 0$ and $C_g^- < \infty$). If the wavelet is localized in time and frequency, admissibility (with respect to all frequencies) is equivalent to the oscillation condition (Holschneider, 1995; Mallat, 1998)

$$\int_{-\infty}^{+\infty} g(t)dt = 0. \tag{A-6}$$

The wavelet transform with respect to an admissible wavelet is a bounded operator from $L^2(\mathbb{R})$ to $L^2(H, dbda/a)$:

$$\int_0^{\infty} \frac{da}{a}\int_{-\infty}^{+\infty} db|\mathcal{W}_g s(b,a)|^2 \le \max\{C_g^+, C_g^-\}\int |s(t)|^2 dt. \tag{A-7}$$

In the case where $C_g^+ = C_g^- = C_g$, we have equality in the above formula. Furthermore, if $C_g > 0$, the energy of the wavelet is conserved up to a constant factor so that the wavelet transform of a signal $s'(t)$ may be inverted by a scalar multiple of its adjoint, which is a wavelet synthesis (Holschneider, 1995)

$$\mathcal{M}_g s'(b,a) = \int_0^{\infty} \frac{da}{a}\int_{-\infty}^{+\infty} db\frac{1}{a} g\left(\frac{t-b}{a}\right) s'(b,a), \tag{A-8}$$

where $\mathcal{M}_g$ denotes the inverse wavelet transform operator. We have $C_g^{-1}\mathcal{M}_g\mathcal{W}_g = 1$, or more explicitely,

$$s(t) = \frac{1}{C_g}\int_0^{\infty} \frac{da}{a}\int_{-\infty}^{+\infty} db\frac{1}{a} g\left(\frac{t-b}{a}\right)\mathcal{W}_g s(b,a). \tag{A-9}$$

For a general admissible g (i.e., if $C_g^+ \neq C_g^-$) we have

$$\mathcal{M}_g\mathcal{W}_g = \frac{1}{2}\left[(C_g^- + C_g^+)1 + \frac{i}{2}(C_g^+ - C_g^-)\mathcal{H}\right], \tag{A-10}$$

where $\mathcal{H}: s(\omega) \mapsto -i\,\mathrm{sign}(\omega)s(\omega)$ is the Hilbert transform.

Note that a progressive wavelet (one whose Fourier transform $\hat{g}(\omega)$ vanishes for $\omega < 0$) cannot be admissible in the above sense because $C_g^- = 0$. Rather, it is only admissible with respect to positive frequencies, and the formulas have to be reinterpreted appropriately. Depending on the signal type, three cases must be considered: general-complex signal, progressive-complex signal, and real-valued signal.

General-complex signal

In a general complex-signal case, no information about the negative frequencies of s is contained in the wavelet transform because only its positive frequency part

$$s^+(t) = \frac{1}{2}(1 + i\mathcal{H})s(t) = \frac{1}{2\pi}\int_0^{\infty} e^{i\omega t}\hat{s}(\omega)d\omega \tag{A-11}$$

is analyzed, so that

$$\mathcal{W}_g s(b,a) = \mathcal{W}_g s^+(b,a). \tag{A-12}$$

Accordingly, applying the inversion formula does not recover s, but rather its positive frequency part

$$\mathcal{M}_g\mathcal{W}_g s = C_g^+ s^+. \tag{A-13}$$

Progressive-complex signal

If the signal itself is progressive (i.e., it contains only positive frequencies), then $s^+ = s$ and the wavelet transform contains all information about s.

Real-valued signal

In case the signal takes only real values $s(t) \in \mathbb{R}$, no information is lost using a progressive wavelet for the analysis. We now have

$$s = 2\Re s^+, \quad \text{and } \|s\|^2 = 2\|s^+\|^2. \tag{A-14}$$

We have for the energy conservation,

$$\|\mathcal{W}_g s\|^2_{L^2(H,dbda/a)} = \frac{C_g}{2}\|s\|^2, \tag{A-15}$$

and for the inversion,

$$s = \frac{2}{C_g}\Re\mathcal{M}_g\mathcal{W}_g s. \tag{A-16}$$

The same considerations apply to the case of a regressive wavelet.

In our numerical applications, we will consider the widely used Morlet wavelet consisting of a plane wave modulated by a Gaussian

$$g^{\pm}(t) = e^{\pm i\omega_0 t}e^{-t^2/2\sigma^2}. \tag{A-17}$$

Strictly speaking, the Morlet wavelet is neither progressive, regressive, nor admissible but can be considered numerically equivalent to a progressive or regressive wavelet when $\sigma > 5$. Note that $1/\sigma = \Delta\omega/\omega = \Delta f/f$ is the constant relative-frequency resolution defined in equation A-2.

REFERENCES

Abdu-Jauwad, S. H., and M. F. Khène, 2000, Two-dimensional wavelet-based ground roll filtering: 70th Annual International Meeting, SEG, Expanded Abstracts, 2107–2110.

Bard, P. Y., 1998, Microtremor measurements: A tool for site effect estimation? Proceedings of the Second International Symposium on the Effect of Surface Geology on Seismic Motion, 25–33.

Deighan, A. J., and D. R. Watts, 1997, Ground-roll suppression using the wavelet transform: Geophysics, **62**, 1896–1903.

Gherasim, M., C. Hoelting, and K. Marfurt, 2004, Fort Worth Basin — 2-D elastic synthetic depth model: 74th Annual International Meeting, SEG, Expanded Abstracts, 1893–1896.

Herrmann, R. B., 1996, Computer programs in seismology: Saint Louis University, Version 3.0.

Holschneider, M., 1995, Wavelets: an analysis tool: Clarendon Press.

Lachet, C., and P. Y. Bard, 1994, Numerical and theoretical investigations on the possibilities and limitations of Nakumara's technique: Journal of Physical Earth, **42**, 377–397.

Li, X. L., and S. Crampin, 1991, Complex component analysis of shear wave splitting: theory: Geophysical Journal International, **107**, 597–604.

Mallat, S., 1998, A wavelets tour of signal processing: Academic Press Inc.

Morozov, I. B., and S. B. Smithson, 1996, Instantaneous polarization attributes and directional filtering: Geophysics, **61**, 872–881.

Ohrnberger, M., F. Scherbaum, F. Krüger, R. Pelzing, and S. K. Reamer, 2003, How good are shear wave velocity models obtained from inversion of ambient vibrations in the Lower Rhine Embayment (N.W. Germany): Bollettino di Geofisica Teorica e' Applicata, 45, 215–232.

Rene, R. M., J. L. Fitter, P. M. Forsyth, K. Y. Kim, D. J. Murray, J. K. Walters, and J. D. Westerman, 1986, Multicomponent seismic studies using complex trace analysis: Geophysics, **51**, 1235–1251.

Scherbaum, F., K. G. Hinzen, and M. Ohrnberger, 2003, Determination of shallow shear wave velocity profiles in the Cologne/Germany area using ambient vibration: Geophysical Journal International, **152**, 597–612.

Shieh, C. F., and R. B. Herrmann, 1990, Ground roll: Rejection using polarization filters: Geophysics, **55**, 1216–1222.

Smith, B. C., and S. H. Ward, 1974, On the computation of polarization ellipse parameters: Geophysics, **39**, 867–869.

Taner, M. T., F. Koehler, and R. E. Sheriff, 1979, Complex seismic trace analysis: Geophysics, **44**, 1041–1063.

Torrence, C., and G. P. Compo, 1998, A practical guide to wavelet analysis: Bulletin of American Meteorological Society, **79**, 61–78.

Torrésani, B., 1995, Analyse continue par ondelletes: CNRS Editions.